AIMS Mathematics, 11(3): 5648–5668.
DOI: 10.3934/math.2026232
Received: 12 December 2025
Revised: 22 February 2026
Accepted: 02 March 2026
Published: 05 March 2026

https://www.aimspress.com/journal/Math

Research article

Dynamics and bifurcation phenomena of a tri-hybrid nanofluid model in a curved channel

Mashael A. Aljohani* **and Eman D. Abou Elela**

Department of Mathematics and Statistics, College of Science in Yanbu, Taibah University, Yanbu Governorate, Saudi Arabia

* **Correspondence:** Email: masjohani@taibahu.edu.sa.

Abstract: In this paper, we present a novel approach to characterize the flow and heat transfer characteristics of a tri-hybrid nanofluid (Blood + TiO_2 + Al_2O_3 + Cu) through a curved, thermally heated channel using analytical and numerical frameworks based on a dynamical system. Dynamical system theory enables systematic identification and analysis of fundamental flow phenomena, including equilibrium states, stability, and bifurcations, which are often difficult to capture with traditional methods. Long-wavelength and low-Reynolds reductions yield analytical flow fields, from which the nonlinear dynamical system was constructed. The analytical determination of the general equilibrium points was complicated by the channel geometry and the strong nonlinearity of the model; therefore, a numerical approach based on domain decomposition techniques was adopted to overcome these difficulties. Saddle-node bifurcations, periodic orbits, and heteroclinic orbits provide a framework to characterize recirculating flows and the transitions between different flow states. The impact of physical properties and nanoparticle characteristics, which affect both global and local bifurcation behavior, was also examined. As a novel result, we revealed multiple equilibrium points with distinct bifurcation behaviors, capturing key fluid motion phenomena, such as trapping, governed by the channel geometry and tri-hybrid nanofluid properties. Our results, based on a dynamical systems analysis, refine and extend previous studies by clarifying the stability of equilibrium solutions, identifying key bifurcation regimes, and revealing the underlying nonlinear flow behavior.

Keywords: nonlinear dynamics; trapping phenomena; multiple-equilibria computation; flow bifurcation; peristaltic motion; numerical simulation
Mathematics Subject Classification: 34C23, 34C37, 37M20, 37N10, 76-10

1. Introduction

In recent years, several theoretical, computational, and experimental studies have investigated nanofluid dynamics and transport phenomena, including flow, heat, and mass transfer, because of their superior thermal properties compared to those of conventional fluids. The concept of nanofluids was first introduced by Choi [1], representing a pivotal advancement in the field. According to [2], the authors examined the thermal and hydrodynamic performance of hybrid nanofluids flowing through twisted oval channels that are uniform and non-uniform. The study reported in [3] explored the transport dynamics of a reactive hybrid nanofluid with gyrotactic microbes over a curved oscillating boundary embedded in a spatially heterogeneous porous medium. Du et al. [4] conducted an experimental study on the effects of nanoparticle concentration and surfactants on nanofluid pool boiling, showing how the nanoparticle concentration optimized heat transfer performance and how nanoparticle deposition enhanced surface wetting and roughness.

The addition of three nanoparticles, known as ternary hybrid (also called tri-hybrid) nanofluid (THNF), to a base fluid has proven essential for improving the performance and reliability of heat transfer applications. It was demonstrated in [5, 6] that THNF enhanced heat transfer, improved rheological properties, and increased thermal conductivity in fluid flow dynamics. A comprehensive review of results related to the thermophysical properties, such as thermal conductivity, viscosity, density, and specific heat, as well as the heat-transfer and flow characteristics of hybrid nanofluids used in various heat exchangers was presented in [7]. The authors in [8] investigated the thermal heat transfer behavior of THNF composed of single-walled carbon nanotubes, multi-walled carbon nanotubes, and iron-oxide nanoparticles by employing an intelligent Levenberg–Marquardt neural-network framework integrated with the finite element method, with special emphasis on entropy generation. The results of the dual solutions of THNF flow composed of alumina, copper, and titania nanoparticles dispersed in a water-based fluid, examined through numerical treatment of a reduced model and complemented by a stability analysis to identify physically realizable solutions, were reported in [9].

Stagnation point (also called an equilibrium point, or steady-state solutions) flows occur when a fluid approaches a location in the flow field where its velocity reduces to zero, leading to the conversion of kinetic energy into pressure. The formation of patterns and the emergence of complex flow structures around multiple stagnation point flows make it essential to develop a systematic approach to investigate and highlight these phenomena. To rationalize pattern formation in fluid flows, dynamical systems theory is an essential tool, and it has been successfully applied to problems such as the generalization of classical two-dimensional Kolmogorov flow [10]. The steady-state solutions were analyzed using both numerical and analytical methods to assess their stability and explore how variations in parameters, such as forcing amplitude or Reynolds number, induce bifurcations, leading to structural changes in the flow, including pattern formation and flow reorganization. In [11], weakly nonlinear analysis and bifurcation theory were used to find the patterns that originate and remain under specified conditions. This extended the classical study of convection pattern creation to non-Newtonian fluids. Further, the application of dynamical systems and bifurcation theory [12, 13] to fluid mechanics, nonlinear optics [14], and neural differential systems [15] has provided a powerful analytical and numerical framework. This framework enables the elucidation of mechanisms governing complex flow transitions, stability characteristics, and the emergence of structured patterns in nonlinear transport systems [16–18]. Establishing the governing motion equations in a dynamical-systems

framework makes it easier to characterize fixed points, periodic flow routes, and separatrix structures that determine the system's global behavior. Bifurcation theory offers a framework for classifying streamline pattern transitions, such as shifts between forward, backward, and trapped flow, as codimension-one equilibrium bifurcations in peristaltic flow systems involving various fluid types. This connects local dynamical shifts to the global transport behavior of the system. In [19] the authors investigated the peristaltic motion of a Bingham viscoplastic fluid under electroosmotic effects in a geometrically intricate wavy microchannel. The findings demonstrated the model's capability to capture key peristaltic transport features of the Bingham fluid, both when symmetric flow conditions are present and when they are absent. Several research works [19–28] modeled peristaltically produced flows, important to diverse biological and biomedical applications and occurring in variously designed channels, as dynamical systems, discovering equilibrium points and examining their stability under modifying critical parameters. These studies used local and global bifurcation analysis to demonstrate how parameter changes impact the streamline topology and influence bolus development.

To the best of our knowledge, bifurcation results for THNF (Blood + TiO_2 + Al_2O_3 + Cu) flow in a curved channel have not yet been presented in the literature. This study therefore offers a novel contribution by applying bifurcation theory to this configuration for the first time. The mathematical model representing THNF incorporates high heat-transfer capability, good dispersion stability, and acceptable viscosity, all arising from the synergistic interaction of the three types of nanoparticles. An exact analytical solution for the stream function and velocity components in curvilinear coordinates is obtained for the peristaltic motion of the THNF, providing the basis for a nonlinear dynamical system. The analytical investigation of equilibrium points is significantly complicated by the complex geometry of the channel and the strong nonlinearity of the model. To address these challenges, we employ a numerical approach based on domain decomposition techniques, which enables us to divide the flow domain into smaller subdomains, compute the equilibrium points within each subdomain, and subsequently analyze their stability. This method also facilitates the visualization of flow patterns and streamlines near the equilibrium points, providing deeper insight into the system's dynamical behavior, such as the existence and stability of equilibrium solutions, bifurcation structures, and transitions between different flow states. It also highlights the influence of the physical parameters, such as the nanoparticle volume fraction and the curvature parameter. Varying the system parameters classifies the equilibrium points into saddle-node, periodic, or heteroclinic orbits, causing changes in the basins of attraction and the appearance or disappearance of trapping zones. The catheter radius ratio, amplitude ratio, and flow rate strongly affect the streamline bifurcation patterns and overall flow dynamics in the curved peristaltic channel.

The paper is organized as follows: Section 2 presents the problem geometry and mathematical model of the THNF, derives the analytical solution, and discusses the associated thermophysical properties. In Section 3, dynamical systems theory is applied to identify equilibrium points using analytical and numerical methods based on domain decomposition techniques, assess their stability, and characterize the resulting streamline topology in the curved channel. Section 4 presents the dynamical system results, highlighting the effects of key physical parameters and tri-hybrid nanoparticles, relative to nanofluids and hybrid nanofluids—on equilibrium point stability, trapping zone formation, and streamline evolution in the curved channel, providing insight into complex flow behavior under physiological conditions. The final section summarizes the main findings, emphasizing the role of the proposed model in capturing flow behavior within the curved channel and offering

insights into complex fluid transport.

2. Model formulation and thermophysical properties

Let the velocity field be defined as $\tilde{\mathbb{V}} = (\tilde{\mathbb{U}}(\tilde{\mathcal{R}}, \tilde{\mathbb{Z}}, \tilde{t}), \tilde{\mathbb{W}}(\tilde{\mathcal{R}}, \tilde{\mathbb{Z}}, \tilde{t}), 0)$. Here, $\boldsymbol{\tau}$ is the Cauchy stress tensor, C_p the specific heat, K the thermal conductivity, r the fluid density, $\tilde{\mathbb{T}}$ the temperature, Q_0 the parameter of heat generation (or absorption), and g the gravitational acceleration. The governing flow equations are then expressed as follows [29]:

$$\nabla.\tilde{\mathbb{V}} = 0, \tag{2.1}$$

$$\frac{d\tilde{\mathbb{V}}}{d\tilde{t}} = \frac{1}{\rho}\nabla.\boldsymbol{\tau} - g\beta(\tilde{\mathbb{T}} - \tilde{\mathbb{T}}_1), \tag{2.2}$$

$$\frac{d\tilde{\mathbb{T}}}{d\tilde{t}} = \frac{K}{\rho C_p}\nabla^2\tilde{\mathbb{T}} + \frac{Q_0}{\rho C_p}, \tag{2.3}$$

where Eqs (2.1) to (2.3) refer to the continuity, momentum, and energy equations, respectively. This study examines the bifurcation and flow dynamics of a tri-hybrid nanofluid (TiO_2-Al_2O_3-Cu/blood) in a lubricated curved concentric channel. In line with the studies of [29, 30], the stress tensor is assumed to vary linearly with the rate of deformation, and the base fluid is treated as Newtonian, which is a common assumption for tri-hybrid nanofluids. Although blood inherently exhibits non-Newtonian behavior, a Newtonian approximation is employed for analytical simplicity and to highlight the influence of nanoparticles on the flow characteristics. The analysis is carried out in a curvilinear coordinate system $(\tilde{\mathcal{R}}, \tilde{\mathbb{Z}})$, where $\tilde{\mathcal{R}}$ and $\tilde{\mathbb{Z}}$ denote the radial and axial directions, respectively. The mathematical formulation for the sinusoidal deformation of the inner and outer walls is given as follows:

$$\begin{aligned} \bar{H}_u(\tilde{t}, \tilde{\mathbb{Z}}) &= a_0 + b_0 \sin\left(\frac{2\pi}{\lambda}(\tilde{\mathbb{Z}} - c\tilde{t})\right), \\ \bar{H}_l(\tilde{t}, \tilde{\mathbb{Z}}) &= n\bar{H}_u(\tilde{t}, \tilde{\mathbb{Z}}) = m\left(a_0 + b_0 \sin\left(\frac{2\pi}{\lambda}(\tilde{\mathbb{Z}} - c\tilde{t})\right)\right), m \in [0, 1], \end{aligned} \tag{2.4}$$

where (a_0, ma_0) corresponds to the mean radii of the inner and outer walls, (b_0, mb_0) indicates the deformation amplitudes, λ is the wavelength of the peristaltic wave, and c denotes its propagation speed. The flow domain of the THNF model is illustrated in Figure 1. The fluid consists of a base Newtonian fluid with three types of nanoparticles.

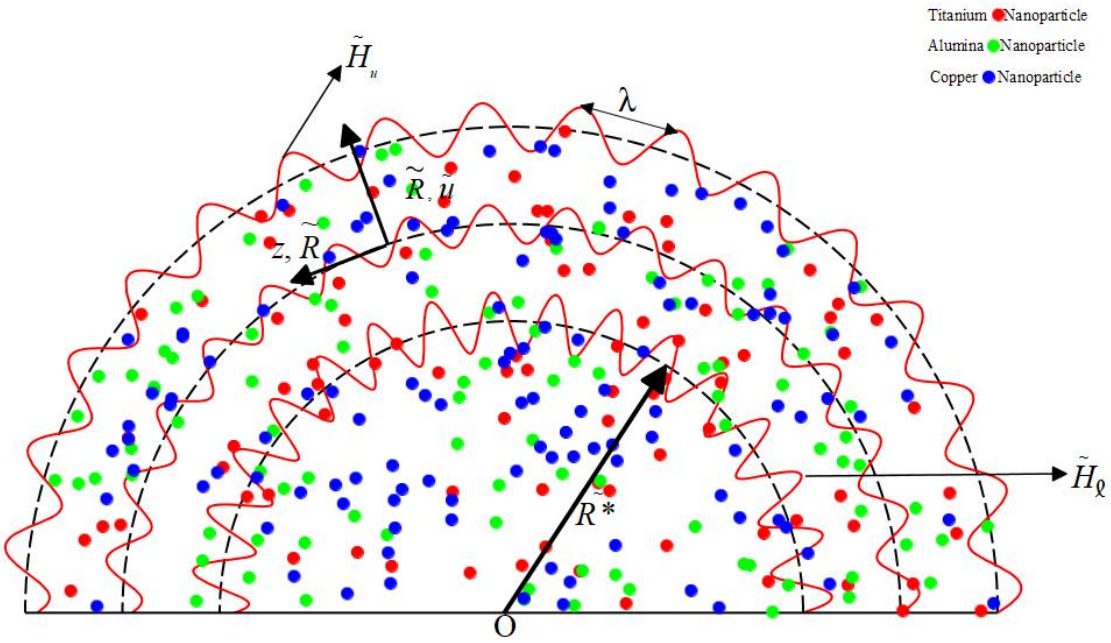

Figure 1. Geometry of the tri-hybrid nanofluid (THNF) model.

The above Eqs (2.1)–(2.3) are reformulated to represent the governing equations of THNF [8, 29] in curvilinear coordinates.

$$\frac{\partial}{\partial \tilde{\mathcal{R}}}\left(\tilde{\mathcal{R}}_c \tilde{\mathbb{U}}\right) + \mathcal{R}^* \frac{\partial \tilde{\mathbb{W}}}{\partial \tilde{\mathbb{Z}}} = 0, \tag{2.5}$$

$$\left[\frac{\rho_{\text{th}}}{\mu_{\text{th}}}\left(\frac{\partial}{\partial \tilde{t}} + \tilde{\mathbb{U}}\frac{\partial}{\partial \tilde{\mathcal{R}}} + \frac{\tilde{\mathcal{R}}^* \tilde{\mathbb{W}}}{\tilde{\mathcal{R}}_c}\frac{\partial}{\partial \tilde{\mathbb{Z}}}\right) - \left(\frac{1}{\tilde{\mathcal{R}}_c}\frac{\partial}{\partial \tilde{\mathcal{R}}}\left(\tilde{\mathcal{R}}_c \frac{\partial}{\partial \tilde{\mathcal{R}}}\right) + \left(\frac{\tilde{\mathcal{R}}^*}{\tilde{\mathcal{R}}_c}\right)^2 \frac{\partial^2}{\partial \tilde{\mathbb{Z}}^2} - \frac{1}{\tilde{\mathcal{R}}_c^2}\right)\right]\tilde{\mathbb{U}} + \frac{1}{\mu_{\text{th}}}\frac{\partial \tilde{\mathcal{P}}}{\partial \tilde{\mathcal{R}}}$$
$$= \frac{\rho_{\text{th}}}{\mu_{\text{th}}}\left(\frac{\tilde{\mathbb{W}}}{\tilde{\mathcal{R}}_c} - \frac{2\tilde{\mathcal{R}}^*}{\tilde{\mathcal{R}}_c^2}\frac{\partial}{\partial \tilde{\mathbb{Z}}}\right)\tilde{\mathbb{W}}, \tag{2.6}$$

$$\left[\frac{\rho_{\text{th}}}{\mu_{\text{th}}}\left(\frac{\partial}{\partial \tilde{t}} + \tilde{\mathbb{U}}\frac{\partial}{\partial \tilde{\mathcal{R}}} + \frac{\tilde{\mathcal{R}}^* \tilde{\mathbb{W}}}{\tilde{\mathcal{R}}_c}\frac{\partial}{\partial \tilde{\mathbb{Z}}}\right) - \left(\frac{1}{\tilde{\mathcal{R}}_c}\frac{\partial}{\partial \tilde{\mathcal{R}}}\left(\tilde{\mathcal{R}}_c \frac{\partial}{\partial \tilde{\mathcal{R}}}\right) + \left(\frac{\tilde{\mathcal{R}}^*}{\tilde{\mathcal{R}}_c}\right)^2 \frac{\partial^2}{\partial \tilde{\mathbb{Z}}^2} - \frac{1}{\tilde{\mathcal{R}}_c^2}\right)\right]\tilde{\mathbb{W}} + \frac{\tilde{\mathcal{R}}^*}{\mu_{\text{th}}\tilde{\mathcal{R}}_c}\frac{\partial \tilde{\mathcal{P}}}{\partial \tilde{\mathbb{Z}}}$$
$$= -\frac{\rho_{\text{th}}}{\mu_{\text{th}}}\left(\frac{\tilde{\mathbb{W}}}{\tilde{\mathcal{R}}_c} - \frac{2\tilde{\mathcal{R}}^*}{\tilde{\mathcal{R}}_c^2}\frac{\partial}{\partial \tilde{\mathbb{Z}}}\right)\tilde{\mathbb{U}} + \frac{(\rho\beta)_{\text{th}}}{\mu_{\text{th}}} g(\tilde{\mathbb{T}} - \tilde{\mathbb{T}}_0), \tag{2.7}$$

$$\left[\frac{(\rho C_p)_{\text{th}}}{K_{\text{th}}}\left(\frac{\partial}{\partial \tilde{t}} + \tilde{\mathbb{U}}\frac{\partial}{\partial \tilde{\mathcal{R}}} + \frac{\tilde{\mathcal{R}}^* \tilde{\mathbb{W}}}{\tilde{\mathcal{R}}_c}\frac{\partial}{\partial \tilde{\mathbb{Z}}}\right) - \left(\left(\frac{\tilde{\mathcal{R}}^*}{\tilde{\mathcal{R}}_c}\right)^2 \frac{\partial^2}{\partial \tilde{\mathbb{Z}}^2} + \frac{1}{\tilde{\mathcal{R}}_c}\frac{\partial}{\partial \tilde{\mathcal{R}}} + \frac{\partial^2}{\partial \tilde{\mathcal{R}}^2}\right)\right]\tilde{\mathbb{T}} = \frac{1}{K_{\text{th}}} Q_0. \tag{2.8}$$

In this formulation, $\tilde{\mathcal{R}}_c = \tilde{\mathcal{R}} + \tilde{\mathcal{R}}^*$, and $(\tilde{\mathbb{U}}, \tilde{\mathbb{W}})$ represents the velocity components in the $\tilde{\mathcal{R}}$ and $\tilde{\mathbb{Z}}$ directions. In addition, $\tilde{\mathbb{T}}$ is the temperature, $\tilde{t}$ is the time variable, and $\tilde{\mathcal{P}}$ denotes the pressure.

Here, the coordinate transformation equations are introduced to relate the physical and curvilinear frames of reference.

$$\bar{r} = \tilde{\mathcal{R}}, \quad \bar{z} = \tilde{\mathbb{Z}} - c\tilde{t}, \quad \bar{P} = \tilde{\mathcal{P}}, \quad \bar{W} = \tilde{\mathbb{W}} - c, \quad \bar{U} = \tilde{\mathbb{U}} \tag{2.9}$$

The principal dimensionless variables and parameters associated with the present problem [6, 29] are defined as follows:

$$\xi = \frac{\bar{r}}{a_0}, \quad z = \frac{\bar{z}}{\lambda}, \quad U = \frac{\lambda \bar{U}}{c a_0}, \quad W = \frac{\bar{W}}{c}, \quad P = \frac{\bar{P} a_0^2}{\mu_{\rm f} \lambda c}, \quad \delta = \frac{a_0}{\lambda}, \quad k = \frac{\tilde{\mathcal{R}}^*}{a_0}, \Theta = \frac{\tilde{\mathbb{T}} - \tilde{\mathbb{T}}_0}{\tilde{\mathbb{T}}_1 - \tilde{\mathbb{T}}_0},$$
$$Re = \frac{c a_0 \rho_{\rm f}}{\mu_{\rm f}}, \quad Gr = \frac{(\tilde{\mathbb{T}}_1 - \tilde{\mathbb{T}}_0) g a_0^2 (\rho\beta)_{\rm f}}{c\, \mu_{\rm f}}, \tag{2.10}$$

where $\Phi = \frac{b}{a}$ is the amplitude ratio. The formulas for the thermophysical properties, where $\rho_{\rm th}$ denotes the density of the THNF, $\mu_{\rm th}$ its viscosity, $K_{\rm th}$ its thermal conductivity, and $(\rho C_p)_{\rm th}$ its effective heat capacity, are listed below.

$$(\rho C_p)_{\rm th} = \sum_{i=f,t,a,c} \phi_i (\rho C_p)_i, \phi_f = 1 - \sum_{i=t,a,c} \phi_i, \quad \frac{\mu_f}{\mu_{th}} = \sum_{i=t,a,c} (1-\phi_i)^{2.5},$$
$$\rho_{\rm th} = (1-\phi_t)\Big[(1-\phi_a)\big((1-\phi_c)\rho_f + \phi_c \rho_c\big) + \phi_a \rho_a\Big] + \phi_t \rho_t,$$
$$(\rho\beta)_{\rm th} = (1-\phi_c)\Big[(1-\phi_a)\big((1-\phi_t)(\rho\beta)_f + \phi_t (\rho\beta)_t\big) + \phi_a (\rho\beta)_a\Big] + \phi_c (\rho\beta)_c.$$

Various standard models have been developed to estimate the effective thermal conductivity ($K_{{\rm etc},i}$) of composite nanomaterials. A detailed discussion of these models can be found in [31–33]. The effective thermal conductivity of the tri-hybrid nanofluid is determined using the general recursive Maxwell model [6, 34].

$$K_{{\rm etc},i} = K_{{\rm etc},i-1} \left(\frac{K_i + 2K_{{\rm etc},i-1} - 2\phi_i (K_{{\rm etc},i-1} - K_i)}{K_i + 2K_{{\rm etc},i-1} + \phi_i (K_{{\rm etc},i-1} - K_i)} \right), \quad K_{{\rm etc},0} = K_f$$

We present it here in its explicit three-step recursive form as follows:

$$K_{{\rm etc},1} = K_f \left(\frac{K_T + 2K_f - 2\phi_T (K_f - K_T)}{K_T + 2K_f + \phi_T (K_f - K_T)} \right),$$
$$K_{{\rm etc},2} = K_{{\rm etc},1} \left(\frac{K_A + 2K_{{\rm etc},1} - 2\phi_A (K_{{\rm etc},1} - K_A)}{K_A + 2K_{{\rm etc},1} + \phi_A (K_{{\rm etc},1} - K_A)} \right),$$
$$K_{\rm th} = K_{{\rm etc},2} \left(\frac{K_C + 2K_{{\rm etc},2} - 2\phi_C (K_{{\rm etc},2} - K_C)}{K_C + 2K_{{\rm etc},2} + \phi_C (K_{{\rm etc},2} - K_C)} \right),$$

where K_i and ϕ_i are the thermal conductivity and volume fraction of the $i^{\rm th}$ nanoparticle, respectively.

By substituting Eqs (2.9) and (2.10) into Eqs (2.5)–(2.8), and invoking the asymptotic assumptions of long wavelength and low Reynolds number [35], the governing differential equations reduce to the following form.

$$\frac{\partial P}{\partial \xi} = 0, \tag{2.11}$$

$$\frac{\partial P}{\partial z} - \frac{\partial}{\partial \xi}\left(\frac{\xi + k}{k} \frac{\partial W}{\partial \xi} \right) + \frac{1+W}{k(\xi+k)} - G_1 \frac{(\xi+k)\Theta}{k} = 0, \tag{2.12}$$

$$\frac{\partial^2\Theta}{\partial\xi^2}+\frac{1}{\xi+k}\frac{\partial\Theta}{\partial\xi}+G_2=0, \tag{2.13}$$

where $G_1=\frac{(\rho\beta)_{\rm th}}{(\rho\beta)_{\rm f}}Gr$ and $G_2=\frac{(\rho C_p)_{\rm f}}{(\rho C_p)_{\rm th}}\frac{K_{\rm f}}{K_{\rm th}}B$.

The differential Eqs (2.11)–(2.13), incorporating the operator $(W,V)^T=\left(-\partial_\xi,\ \frac{k}{\xi+k}\partial_z\right)\Psi$, are solved analytically subject to the following boundary conditions:

$$\begin{aligned}
&\Psi(z,h_u(z))=\frac{q}{2},\quad \Theta(z,h_u(z))=1,\qquad \left.\frac{\partial\psi(z,\xi)}{\partial\xi}\right|_{\xi=h_u(z)}=1,\\
&\Psi(z,h_l(z))=-\frac{q}{2},\quad \Theta(z,h_l(z))=0,\qquad \left.\frac{\partial\psi(z,\xi)}{\partial\xi}\right|_{\xi=h_l(z)}=1,
\end{aligned} \tag{2.14}$$

where

$$\begin{aligned}
h_u(z)&=1+\phi\sin(2\pi z),\\
h_l(z)&=m+m\phi\sin(2\pi z).
\end{aligned} \tag{2.15}$$

The nonlinear systems (2.11)–(2.13), subject to the boundary conditions (2.14), is solved analytically, yielding explicit expressions for the velocity and pressure fields.

2.1. Derivation of the analytical solution

The governing equation for the temperature distribution is a second-order linear differential equation. To facilitate its solution, we introduce the substitution $\Theta'(z,\xi)=u(\xi)$, which reduces the equation to a first-order ordinary differential equation (ODE):

$$u'+\frac{1}{\xi+k}u=-G_2.$$

Hence,

$$u=\Theta'=-\frac{G_2}{2}(\xi+k)+\frac{A_1(z)}{\xi+k}.$$

By integrating, we obtain the analytical solution to the differential equation governing the temperature distribution is presented in an explicit form as follows:

$$\Theta(z,\xi)=-\frac{G_2}{4}(\xi+k)^2+A_1(z)\ln(\xi+k)+A_2(z), \tag{2.16}$$

where $A_1(z)$ and $A_2(z)$ are obtained by applying the boundary conditions. Therefore,

$$\begin{aligned}
A_1(z)&=\frac{1}{A_3(z)}\left(4+\left(h_l-h_u\right)\left(h_l+2k+h_u\right)G_2\right),\\
A_2(z)&=\frac{1}{A_3(z)}\left(\left(-4-G_2\left(h_l+k\right)^2\right)\ln\left(h_u+k\right)+G_2\ln\left(h_l+k\right)\left(h_u+k\right)^2\right),\\
A_3(z)&=4(\ln(h_l+k)-\ln(h_u+k)).
\end{aligned} \tag{2.17}$$

Differentiation of Eq (2.12) with respect to ξ eliminates the pressure term. Upon setting $W = -\dfrac{\partial \psi}{\partial \xi}$, a fourth-order differential equation is obtained, which can be solved analytically. The general form of the solution to Eq (2.12), incorporating the boundary conditions given in (2.14), is presented below.

$$\Psi(z,\xi) = \check{\mathcal{P}}(z,\xi) + \check{\mathbb{Q}}(z,\xi)\ln(\xi + k) \tag{2.18}$$

where

$$\begin{aligned}\check{\mathcal{P}}(z,\xi) = &-\frac{1}{300}G_1\xi^5 G_2 - \frac{1}{60}G_1\xi^4 G_2 k - \frac{1}{30}G_1\xi^3\left(\frac{50}{9}A_1 - \frac{10}{3}A_2 + G_2 k\right)\\ &+\left[\frac{1}{30}k\left(\frac{50}{3}A_1 + G_2k^2 - 10A_2\right)G_1 - \frac{1}{2}C_3 + \frac{1}{4}C_2\right]\xi^2\\ &+\left[\frac{1}{60}k^2\left(-20A_2 + \frac{100}{3}A_1 + G_2k^2\right)G_1 + 1 + \frac{1}{2700}(1350C_2 - 2700C_3)k\right]\xi\\ &+ C_4 + \frac{1}{4}C_2k^2 - \frac{1}{27}G_1A_1k^3.\end{aligned}$$

$$\check{\mathbb{Q}}(z,\xi) = \frac{G_1A_1}{9}(\xi + k)^3 - \frac{C_2}{2}(\xi + k)^2 - C_1.$$

It is noted that A_1 and A_2, as defined by Eq (2.17), along with $C_1, \ldots, C_4$, are all functions of z, where

$$\begin{aligned}C_1 &= \frac{M_1}{M_2}, M_3 = \mathbb{K}_1^2\left(\ln(\mathbb{K}_1) - \ln(\mathbb{K}_2)\right)\mathbb{K}_2^2, \mathbb{K}_1 = h_u + k, \mathbb{K}_2 = h_l + k,\\ C_2 &= \left(60\,A_1\,G_1\,\mathbb{K}_1^3{\mathbb{K}_2}^2\ln(\mathbb{K}_1) - 60\,A_1\,G_1\,{\mathbb{K}_1}^2\mathbb{K}_2^3\ln(\mathbb{K}_2) - 80\left(\frac{3}{80}\,\mathbb{K}_1^4\mathbb{K}_2^2 G_1\,G_2 + \frac{3}{80}\,\mathbb{K}_1^3\mathbb{K}_2^3 G_1\,G_2\right.\right.\\ &\left.\left. + \mathbb{K}_2^2\left(\frac{3}{80}\,G_2\,\mathbb{K}_2^2 + A_1 - 3/4\,A_2\right)G_1\,\mathbb{K}_1^2 - 9/4\,C_1\,\mathbb{K}_1 - 9/4\,C1\,\mathbb{K}_2\right)(-\mathbb{K}_2 + \mathbb{K}_1)\right)\Big/(180M_3),\end{aligned}$$

$$\begin{aligned}C_3 &= \left(-60\,\mathbb{K}_1^2\left(G_1\,A_1\,\mathbb{K}_2^2\,(\mathbb{K}_1 - \mathbb{K}_1)\ln(\mathbb{K}_2) + \frac{1}{20}\,G_1\,G_2\,\mathbb{K}_2^5 + G_1\left(\frac{4}{3}A_1 - A_2\right)\mathbb{K}_2^3 + 3C_1\right)\ln(\mathbb{K}_1)\right.\\ &\left. + 80\left(\frac{3}{80}\,G1\,\mathbb{K}_1^5 G_2 + G_1\left(-\frac{3}{4}\,A_2 + A_1\right)\mathbb{K}_1^3 + \frac{9}{4}\,C_1\right)\ln(\mathbb{K}_2)\,\mathbb{K}_2^2\right)\Big/(180M_3),\\ C4 &= \frac{1}{2700}\left(-300\,A_1\,G_1\,\mathbb{K}_2^3 + 1350\,C_2\,\mathbb{K}_2^2 + 2700\,C_1\right)\ln(\mathbb{K}_2) + \frac{1}{300}\,G_1\,G_2\,\mathbb{K}_2^5\\ &+ \frac{5}{27}\left(A_1 - \frac{3}{5}\,A_2\right)G_1\,{\mathbb{K}_2}^3 + \frac{1}{2700}\,(1350\,C_3 - 675\,C_2)\,\mathbb{K}_2^2 - \mathbb{K}_2\\ &- \frac{1}{300}\left(\frac{400}{9}\,A_1 - \frac{100}{3}\,A_2 + G_2\,k^2\right)k^3 G_1 + k - 1/2\,q - 1/2\,C_3\,k^2,\end{aligned}$$

$$
\begin{aligned}
M_1 = &-(-10800\ln(\mathbb{K}_1)q - 10800\ln(\mathbb{K}_1)\mathbb{K}_2 - 10800\ln(\mathbb{K}_2)\mathbb{K}_1 + 10800\ln(\mathbb{K}_2)q + 10800\ln(\mathbb{K}_2)\mathbb{K}_2 \\
&- 400A_1G_1\ln(\mathbb{K}_1)\mathbb{K}_2^3 + 1300A_1G_1\ln(\mathbb{K}_1)\mathbb{K}_1^3 - 54\ln(\mathbb{K}_2)G_1{\mathbb{K}_1}^5G_2 - 400\ln(\mathbb{K}_2)G_1{\mathbb{K}_1}^3A_1 \\
&+ 600\ln(\mathbb{K}_2)G_1{\mathbb{K}_1}^3A_2 + 54\ln(\mathbb{K}_2)G_1G2\mathbb{K}_2^5 - 600\ln(\mathbb{K}_2)G_1A_2\mathbb{K}_2^3 + 1300\ln(\mathbb{K}_2)G_1A_1\mathbb{K}_2^3 \\
&- 54\ln(\mathbb{K}_1)G_1G_2\mathbb{K}_2^5 + 600\ln(\mathbb{K}_1)G_1A_2\mathbb{K}_2^3 + 54\ln(\mathbb{K}_1)G_1\mathbb{K}_1^5G_2 - 600\ln(\mathbb{K}_1)G_1\mathbb{K}_1^3A_2 \\
&- 600A_1G_1\mathbb{K}_2^3(\ln(\mathbb{K}_2))^2 - 600G_1\mathbb{K}_1^3A_1(\ln(\mathbb{K}_1))^2 + 1200G_1{\mathbb{K}_1}^2A_1\mathbb{K}_2 + 1200G_1\mathbb{K}_1A_1{\mathbb{K}_2}^2 \\
&+ 45G_1G_2\mathbb{K}_1^3\mathbb{K}_2^2 + 45G_1G_2\mathbb{K}_1^2\mathbb{K}_2^3 - 900G_1{\mathbb{K}_1}^2A_2\mathbb{K}_2 - 900G_1\mathbb{K}_1A_2{\mathbb{K}_2}^2 + 900G_1\mathbb{K}_1^3A_2 \\
&- 45G_1\mathbb{K}_1^5G_2 - 1200G_1\mathbb{K}_1^3A_1 - 45G_1G2\mathbb{K}_2^5 + 900G_1A_2\mathbb{K}_2^3 - 1200A_1G_1\mathbb{K}_2^3 + 10800\ln(\mathbb{K}_1)\mathbb{K}_1 \\
&- 900\ln(\mathbb{K}_1)G_1\mathbb{K}_1A_1\mathbb{K}_2^2 + 600\ln(\mathbb{K}_2)G_1A_1\ln(\mathbb{K}_1)\mathbb{K}_2^3 + 600\ln(\mathbb{K}_2)G_1A_1\ln(\mathbb{K}_1)\mathbb{K}_1^3 \\
&- 900\ln(\mathbb{K}_2)G_1\mathbb{K}_1^2A_1\mathbb{K}_2)\mathbb{K}_2^2\mathbb{K}_1^2, \\
M_2 = &\ 2700\left(-2\mathbb{K}_2\mathbb{K}_1\ln(\mathbb{K}_2) + 2\mathbb{K}_2\mathbb{K}_1\ln(\mathbb{K}_1) - \mathbb{K}_2^2 + {\mathbb{K}_1}^2\right)\left(2\mathbb{K}_2\mathbb{K}_1\ln(\mathbb{K}_2) - 2\mathbb{K}_2\mathbb{K}_1\ln(\mathbb{K}_1)\right. \\
&\left.- {\mathbb{K}_2}^2 + \mathbb{K}_1^2\right).
\end{aligned}
$$

3. Dynamics and bifurcation in patterned flows

In this section, we analyze the nonlinear dynamical behavior of peristaltic flow through a curved channel, revealing complex flow structures and bifurcation phenomena resulting from the interaction between curvature and nonlinear effects. By employing the relations $W = -\frac{\partial\Psi}{\partial\xi}$ and $V = \frac{k}{\xi+k}\frac{\partial\Psi}{\partial z}$, the governing equations are transformed into a system of nonlinear differential equations.

$$
\begin{aligned}
W &= -\frac{\partial\Psi}{\partial\xi} = -\frac{\partial\check{\mathcal{P}}}{\partial\xi} - \frac{\partial\check{\mathbb{Q}}}{\partial\xi}\ln(\xi+k) - \frac{\check{\mathbb{Q}}}{\xi+k} = \boldsymbol{F}_1(\xi,z,\boldsymbol{\gamma}), \\
V &= \frac{k}{\xi+k}\frac{\partial\Psi}{\partial z} = \frac{k}{k+\xi}\left(\frac{\partial\check{\mathcal{P}}}{\partial z} + \frac{\partial\check{\mathbb{Q}}}{\partial z}\ln(\xi+k)\right) = \boldsymbol{F}_2(\xi,z,\boldsymbol{\gamma}),
\end{aligned}
\tag{3.1}
$$

where $\boldsymbol{\gamma}$ is a control parameter, which is a function of $\{k, m, Gr, B, ..\} \in \mathbb{R}^d$.

Equilibrium (stagnation) Points: Consider the above dynamical system (3.1), which can be rewritten as

$$
\dot{X} = F(X;\boldsymbol{\gamma}), \qquad X \in \mathbb{R}^2, \quad \boldsymbol{\gamma} \in \mathbb{R}^d, \tag{3.2}
$$

where $\dot{X} = (W, V)$ denotes the velocity vector of the fluid. The stagnation points $X_s(\boldsymbol{\gamma})$ are determined by solving

$$
F(X_s;\boldsymbol{\gamma}) = 0.
$$

Each solution $X_s(\boldsymbol{\gamma})$ corresponds to a steady state (stagnation) of the system.

Local bifurcation analysis is performed by linearizing the system about the equilibrium point X_s using

$$
X = X_s + \eta,
$$

which leads to the linearized system

$$
\dot{\eta} = \boldsymbol{J}(X_s,\boldsymbol{\gamma})\,\eta, \qquad \boldsymbol{J}(X_s,\boldsymbol{\gamma}) = \frac{\partial F}{\partial X}(X_s;\boldsymbol{\gamma}).
$$

The eigenvalues $\{\lambda_i(\boldsymbol{\gamma})\}_{i=1}^2$ of the Jacobian $\boldsymbol{J}$ are then computed to investigate the local stability and detect bifurcation points of the system.

Lemma 1. *Assume that h_u and h_l are defined by Eq* (2.15)*, with $\frac{\partial h_u}{\partial z} = \frac{\partial h_l}{\partial z} = 0$. If an equilibrium point X_s exists, its stability is determined by the eigenvalues, which in this case are simply the diagonal entries:*

$$\lambda_1 = -\left.\frac{\partial^2 \Psi}{\partial \xi^2}\right|_{X_s}, \qquad \lambda_2 = \left.\frac{k}{k+\xi}\frac{\partial^2 \Psi}{\partial z^2}\right|_{X_s}.$$

The stability of X_s depends on the signs of λ_1 and λ_2, and it can be stable, unstable, or a saddle point.

Proof. Since $\dfrac{\partial h_u}{\partial z} = \dfrac{\partial h_l}{\partial z} = 0$, all first derivatives of the coefficients C_i $(i = 1, \ldots, 4)$ and A_1, A_2 with respect to z vanish when the walls have no axial slope (i.e., $\Psi_z = \Psi_{\xi z} = \Psi_{z\xi} = 0$). Under this condition, the equations in ξ and z become decoupled. Consequently, the Jacobian matrix evaluated at X_s is diagonal, and its eigenvalues are simply the diagonal entries, namely λ_1 and λ_2.

It is important to note that the location and number of equilibrium points can change as the system parameters vary, indicating the occurrence of flow bifurcations. These equilibrium points may appear near the wall, along the centerline, or at any location within the tube, depending on physical parameters such as wave amplitude and curvature. The presence and movement of these points often mark the transition between forward and backward recirculating flow regions and can lead to the formation of trapping zones. The determination of equilibrium points is particularly challenging because the nonlinear interactions inherent in the fluid system lead to intricate coupling between modes and parameters, which often prevents analytical solutions and necessitates the use of numerical techniques. Several software packages, such as `AUTO`, `MatCont`, and those based on pseudo-arclength continuation methods, can be employed to solve $F(X_s; \boldsymbol{\gamma}) = 0$ and continue solution branches. These tools also allow the computation of eigenvalues along the branches to identify and locate bifurcation points.

In short, here we explain the challenge of finding equilibrium points arising from the nonlinear nature of the model.

Proposition 1. *Let $z = \frac{1}{4} + \frac{n}{2},\ n \in \mathbb{Z}$. Then, both h_u and h_l become independent of z and satisfy*

$$h_l = m(1 + \operatorname{sign}(n)\,\phi) = h_u.$$

Therefore,

$$F_2\left(\xi, \frac{1}{4} + \frac{n}{2}, \boldsymbol{\gamma}\right) = 0, \qquad \forall\, \xi, \boldsymbol{\gamma} \in \mathbb{R}.$$

The vector field corresponding to the dynamical system (3.1) is reduced to an equation that involves only a single variable:

$$F_1\left(\xi, \frac{1}{4} + \frac{n}{2}, \boldsymbol{\gamma}\right) = (\xi + k)\big(C_2 \ln(\xi + k) + C_3\big) - 1 + \frac{C_1}{\xi + k}, \tag{3.3}$$

Let $y = \xi + k,\ y > 0$, and then

$$F_1\left(y, \frac{1}{4} + \frac{n}{2}, \boldsymbol{\gamma}\right) = y^2\big(C_2 \ln(y) + C_3\big) - y + C_1 = 0. \tag{3.4}$$

Since this equation contains the product $y^2 \ln(y)$, there is no general closed-form analytic solution in elementary functions. Even when C_2 is small, the perturbation approach begins by neglecting the

$y^2 \ln(y)$ term to obtain the zeroth-order approximation y_0, and then proceeds to compute higher-order corrections in the expansion

$$y \approx y_0 + C_2 y_1 + \cdots .$$

However, this procedure encounters a difficulty related to the convergence of the resulting series, and it applies only to finding a single equilibrium point, whereas the dynamical system is expected to have multiple equilibrium points. Since this approach is ineffective, we introduce an alternative method based on partitioning the domain into small sub-intervals. Accordingly, the equilibrium points are computed using numerical domain decomposition techniques [15].

Definition 1. *Let L denote the wavelength of the traveling wall, and let n_1 and n_2 be non-negative integers specifying the number of wavelengths included upstream and downstream of the reference position $z = 0$, respectively. Then the solution domain in (ξ, z) is defined as:*

$$\Omega = \left\{ (\xi, z) \;\middle|\; -n_1 L \leqslant z \leqslant n_2 L, \;\; h_l(z) \leqslant \xi \leqslant h_u(z) \right\},$$

where h_u and h_l are defined by Eq (2.15)*, with parameters satisfying $0 < m < 1$, $0 < \phi < 1$, denoting the mean radius ratio and the wave-amplitude ratio, respectively.*

To divide the domain into small sectors, let the axial interval $[-n_1 L, n_2 L]$ be divided into N_z subintervals:

$$z_0 = -n_1 L, \quad z_i = z_0 + i\,\Delta z, \quad \Delta z = \frac{(n_1 + n_2)L}{N_z}, \quad i = 0, 1, \ldots, N_z.$$

For each axial slice z_i, divide the radial interval $[h_l(z_i), h_u(z_i)]$ into N_ξ subintervals:

$$\xi_0^{(i)} = h_l(z_i), \quad \xi_j^{(i)} = h_l(z_i) + j\,\Delta\xi_i, \quad \Delta\xi_i = \frac{h_u(z_i) - h_l(z_i)}{N_\xi}, \quad j = 0, 1, \ldots, N_\xi.$$

Then, each small 2D cell is defined as

$$\Omega_{i,j} = \left\{ (\xi, z) \;\middle|\; z_{i-1} \leqslant z \leqslant z_i, \;\; \xi_{j-1}^{(i)} \leqslant \xi \leqslant \xi_j^{(i)} \right\}, \quad i = 1, \ldots, N_z, \;\; j = 1, \ldots, N_\xi.$$

This implies that each sector $\Omega_{i,j}$ can be treated independently when searching for equilibrium points. Initial guesses for each sector are selected using local averages of adjacent grid points, enhancing convergence and promoting comprehensive exploration of the solution space. Moreover, after each iteration we can verify that the updated point remains inside the corresponding sector.

Subsequently, we utilize the MatCont software, built on the MATLAB platform, to compute equilibrium points within each sector $\Omega_{i,j}$, and their associated eigenvalues, and the local streamline patterns in the neighborhoods of these points are visualized to validate the results. The convergence condition in MatCont relies on the Newton correction scheme, whereby a solution is deemed convergent once both the residual norm and the update step meet the specified tolerance thresholds [36]. These points are then collected to analyze their stability and to numerically visualize the local streamline patterns around them.

4. Results and discussion

In this section, we present the results of our dynamical systems analysis of tri-hybrid nanofluid peristaltic transport in curved tubes. The use of dynamical systems theory is especially advantageous because it provides a structured approach to investigating complex flow behaviors. It is particularly useful for identifying and assessing the stability of equilibrium points, detecting bifurcations, and elucidating the mechanisms governing nonlinear interactions within the flow.

The Dynamical system (3.1) depends on several parameters that significantly influence its behavior. Therefore, we analyze the effects of these parameters to identify the specific values that give rise to equilibrium points and induce bifurcations. Such bifurcations correspond to qualitative changes in the stability or structure of the solutions, providing insight into the underlying dynamics of THNF transport in curved tubes.

The simulations are carried out based on the thermophysical properties of the base fluid and THNF nanoparticles, as summarized in Table 1. Figure 2 shows the variation of equilibrium-point positions within the velocity profile $W(z_0, \xi)$, noting that $V(z_0, \xi) = 0$ for all $\xi \in \mathbb{R}$ (Proposition 1). Figure 2(a) presents a comparison between the base and tri-hybrid nanofluids at fixed physical parameter values, while Figure 2(b) illustrates the appearance and disappearance of equilibrium points in the THNF flow with respect to the flow rate parameter.

Table 1. Key thermal and physical properties of the base fluid and THNF nanoparticles [29].

Property	Blood	TiO_2	Al_2O_3	Cu
ρ (kg/m^3)	1063	4250	3970	8933
k (W/m·K)	0.492	8.95	40	401
C_p (J/kg·K)	3594	686	765	385
ϕ	0.96	0.01	0.02	0.01
$\beta \times 10^{-5}$ (K^{-1})	0.18	0.90	0.85	1.67

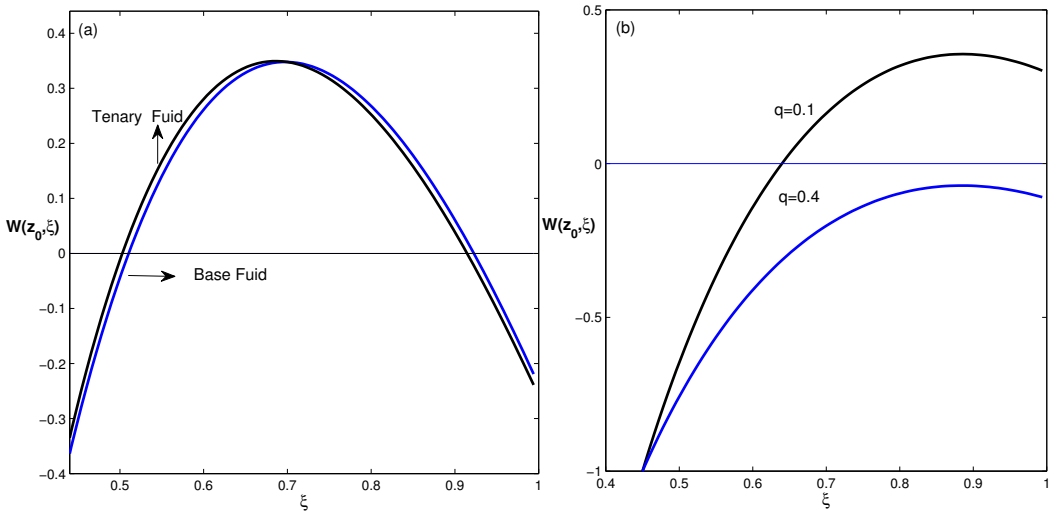

Figure 2. Variation of equilibrium-point positions within the velocity profile $W(z_0, \xi)$ (noting that $V(z_0, \xi) = 0$ for all $\xi \in \mathbb{R}$): (a) comparison between the base and tri-hybrid nanofluids at $k = 0.1$, $Gr = 1$, $B = 2$, $\phi = 0.2$, $q = 0.1$, $m = 0.3$, and $z_0 = \frac{1}{4}$; (b) appearance and disappearance of equilibrium points in the THNF flow with respect to the parameter q at $k = 0.1$ and $\phi = 0.5$.

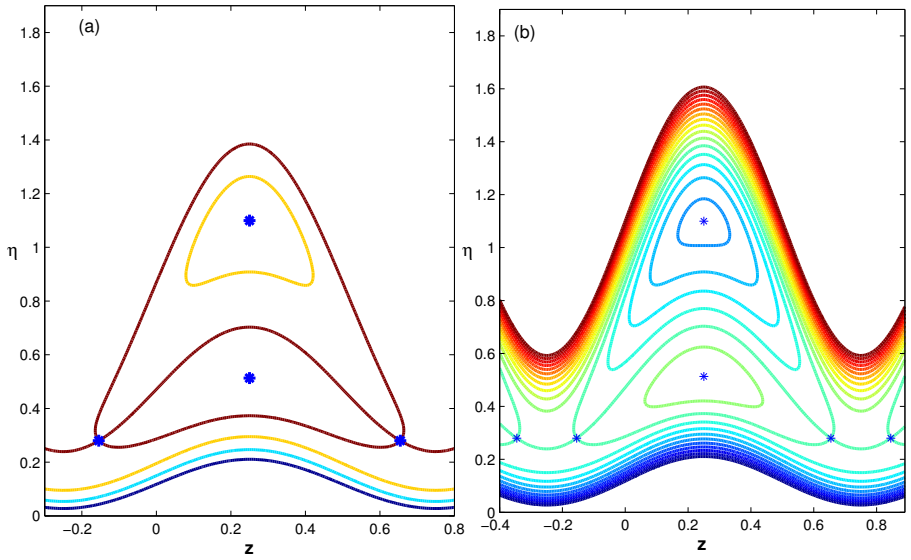

Figure 3. When the buoyancy term in (3.1) becomes zero ($Gr = 0$), complete streamline trapping occurs for the parameters $k = 0.0969$, $m = 0.2$, $q = 0.15$, and $\phi = 0.5$. (a) Heteroclinic connections are shown, and (b) the corresponding streamline topology and trapping zones are illustrated.

With $Gr = 0$, the buoyancy term in (3.1) vanishes, causing the thermal contributions to no longer affect the bifurcation structure of the system. This assumption is justified in microcirculatory blood flow within narrow endoscopic channels, where the flow is primarily driven by peristaltic motion and gravitational effects are negligible. In this situation, the number and locations of equilibrium points are determined solely by geometric factors and other parameter effects. For the parameter set $k = 0.0969$, $m = 0.2$, $q = 0.15$, and $\phi = 0.5$, the heteroclinic connections between the saddle–node points give rise to streamlines that establish fully enclosed trapping zones across the channel, as shown in Figure 3. The dynamical behavior presented in Figure 3 is in agreement with the basic characteristics of peristaltic flow through a curved channel.

On the other hand, the quantity m is defined as the ratio of radii between the catheter and the tube and reflects the level of blockage caused by the catheter. It offers a dimensionless representation of how catheter size affects the available flow area. Figure 4 demonstrates that adjusting this radius ratio modifies the distribution and nature of equilibrium points in the phase space. These modifications arise from streamline bifurcations, which trigger qualitative shifts in the flow structure and its topological characteristics.

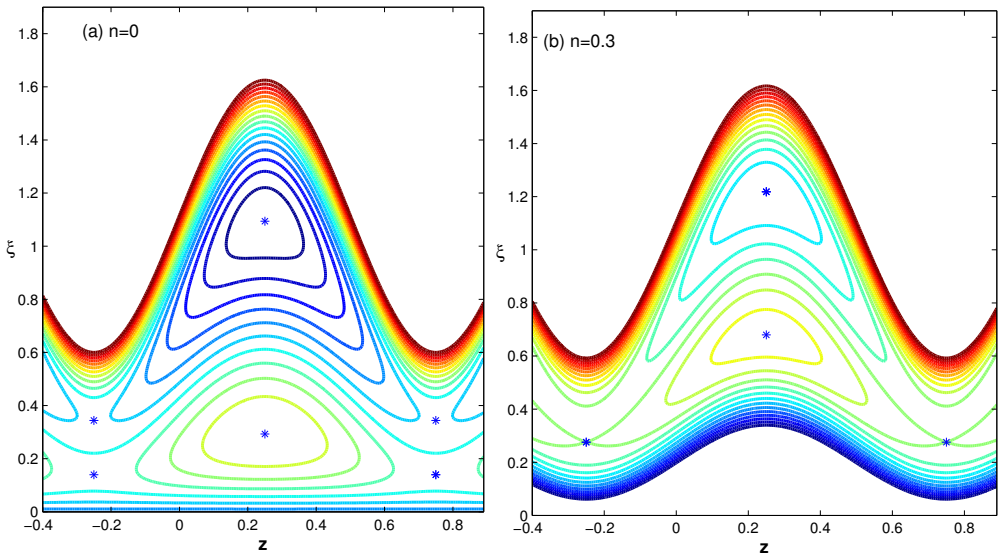

Figure 4. Streamline patterns of THNF transition from four saddle-node points to two connected saddle-node points, with a heteroclinic orbit forming a trapping zone in the lower part of the channel, illustrating the effect of varying the catheter radius ratio at $Gr = B = 1$, $\phi = 0.5$, $q = 0.1$, and $k = 2.01$.

Figure 5 illustrates the evolution of the temperature field for the four examined fluid types—base fluid, nanofluid, hybrid nanofluid, and tri-hybrid nanofluid (THNF)—under the influence of the heat source/sink parameter (B). All temperature profiles exhibit a monotonically decreasing behavior, which is in agreement with the results reported in [29] . For the heat source case ($B = 1$), the base fluid shows the steepest decline, indicating the fastest cooling rate, whereas the THNF experiences the smallest temperature reduction and maintains the highest temperature throughout the domain. In contrast, when ($B = -1$) (heat sink), the behavior reverses: The temperature distributions follow the ordering

for ($B = 1$):

$$\theta_{\text{THNF}} > \theta_{\text{Hybrid fluid}} > \theta_{\text{Nanofluid}} > \theta_{\text{Base fluid}},$$

and for ($B = -1$):

$$\theta_{\text{THNF}} < \theta_{\text{Hybrid fluid}} < \theta_{\text{Nanofluid}} < \theta_{\text{Base fluid}}.$$

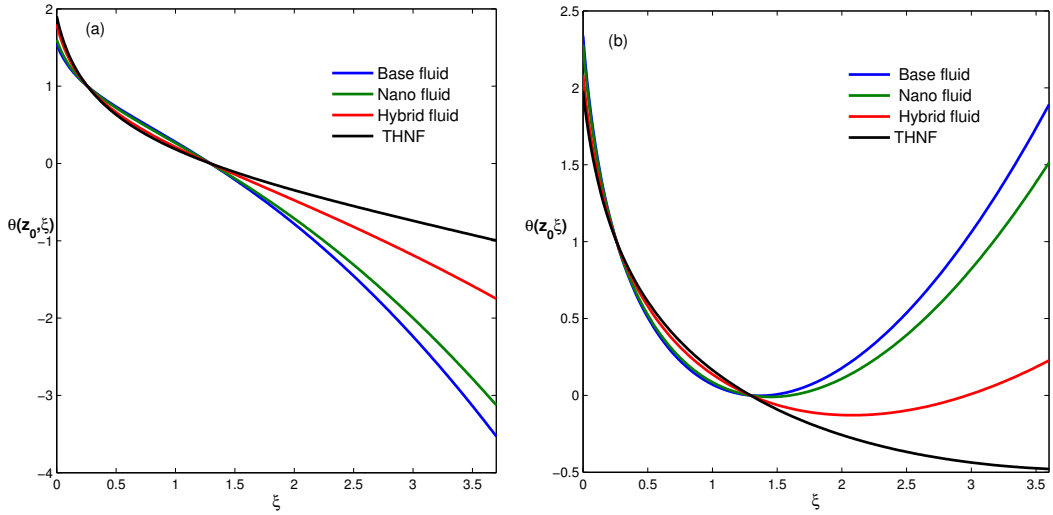

Figure 5. Temperature profile comparing the nanofluid, hybrid nanofluid, and THNF with the base fluid for the heat source/sink parameter B at $k = 0.1, \phi = 0.5, m = 0.2$, and $z_0 = \frac{1}{4}$; (a) $B = 1.0$ and (b) $B = -1.0$.

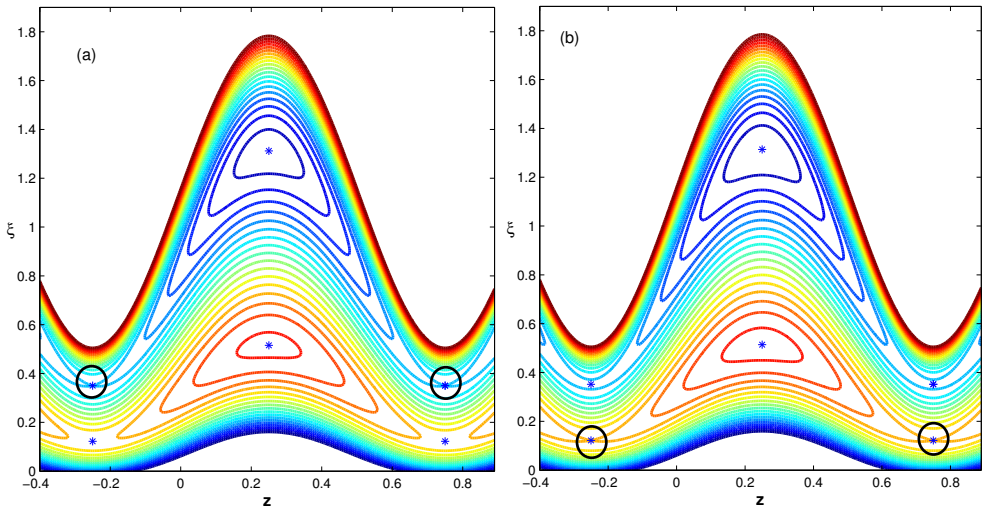

Figure 6. Impact of the THNF flow rate on the trapping zone formed via a heteroclinic orbit, illustrating its transition from the upper to the lower part of the channel at $k = 1$, $\phi = 0.6$, $Gr = 1.0$, $B = -3.0$, and $m = 0.2$; (a) $q = -0.1133$ and (b) $q = -1.0$.

The effect of the THNF flow rate q on the trapping zone associated with a heteroclinic orbit is depicted in Figure 6, revealing a transition of the trapping region from the upper to the lower portion of the channel.

To illustrate the possibility of the trapping zone shifting clearly from the upper to the lower region of the channel, Figure 7 shows that the trapping zone generated by the heteroclinic orbit in THNF flow is highly sensitive to the catheter radius ratio k. For the parameters $q = 0.1133$, $\phi = 0.5$, $Gr = B = 1.0$, and $m = 0.2$, this behavior highlights how variations in k strongly affect the streamline topology and particle confinement, demonstrating the pronounced geometric influence on orbit-induced trapping.

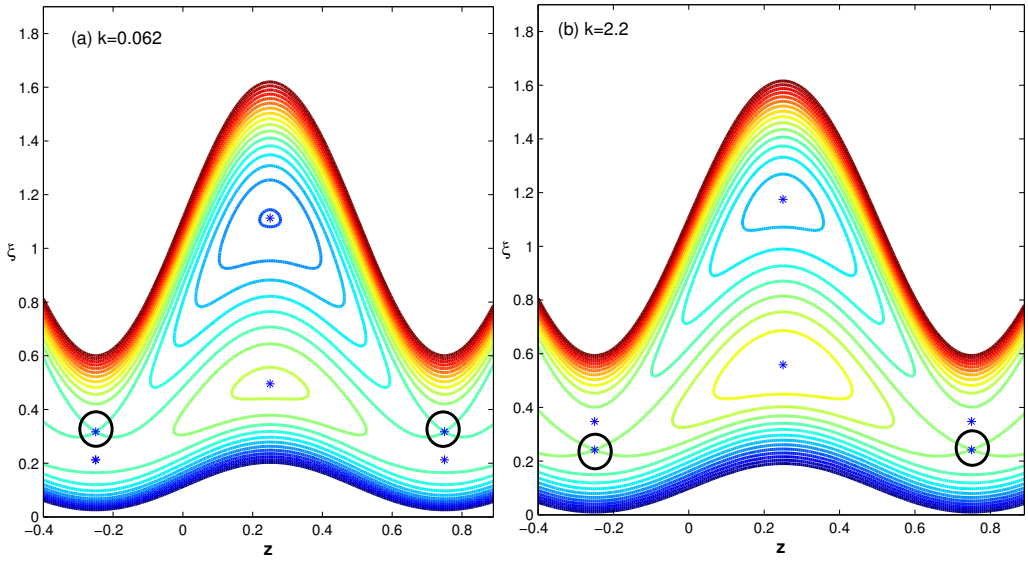

Figure 7. Variation in the trapping zone generated by a heteroclinic orbit in THNF flow as affected by the catheter radius ratio k, highlighting the transition of the trapping zone from the upper to the lower channel region at $q = 0.1133$, $\phi = 0.5$, $Gr = B = 1.0$, and $m = 0.2$.

It is noted that the channel curvature generates centrifugal forces that modify velocity distributions, affecting equilibrium stability and shifting bifurcation points (Figures 4 and 7). The catheter radius ratio k and the parameter m further modify the flow by reducing the effective cross-section and enhancing curvature effects, collectively influencing the locations of equilibrium points as well as the related stability and bifurcation behavior.

Finally, we examine the most complex scenario, in which the heteroclinic orbit in the THNF flow generates a trapping zone that is highly sensitive to changes in the amplitude ratio ϕ. Figure 8 shows that as ϕ varies, new equilibrium points emerge, altering the underlying flow structure and progressively enlarging the trapping zone. Ultimately, this evolution allows the trapping region to expand and occupy the whole channel.

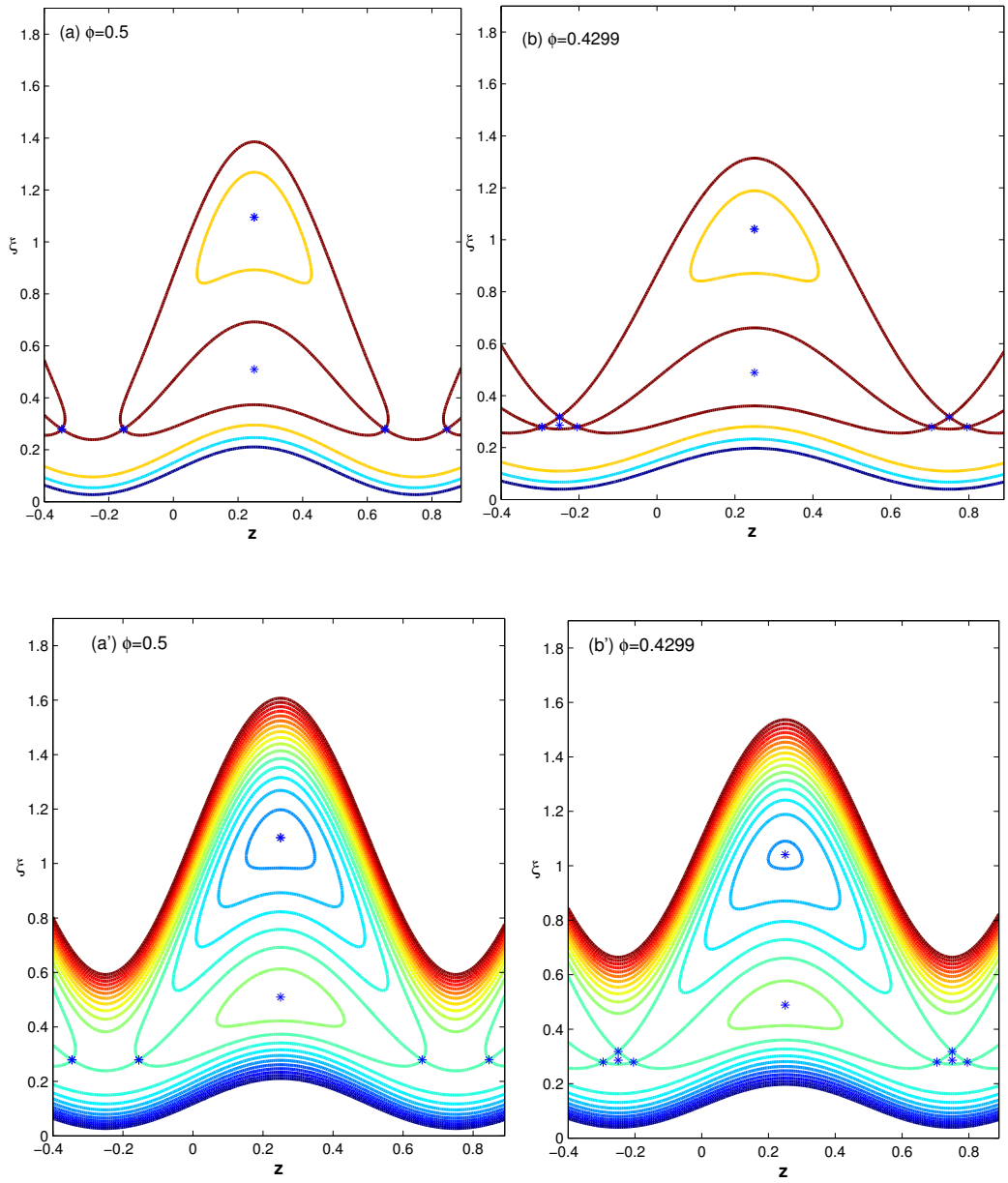

Figure 8. The complex behavior of the trapping zone generated by a heteroclinic orbit in THNF flow is influenced by the amplitude ratio ϕ, whose variation leads to the appearance of new equilibrium points, illustrating how the trapping zone expands to occupy the full channel for the parameter set $q = 0.15$, $k = 0.1028$, $Gr = 2$, $B = 1.0$, and $m = 0.2$. (a) and (b) show different forms of heteroclinic connections, while (a′) and (b′) visualize the corresponding streamline topology and illustrate the trapping zones.

5. Conclusions

In this work, dynamical systems theory, combined with analytical and numerical computational tools, is employed to investigate the behavior of a tri-hybrid nanofluid (Blood + TiO_2 + Al_2O_3 + Cu) flowing through a curved, thermally heated channel. The analysis focuses on streamline patterns, flow transport characteristics, and heat transfer behavior at critical bifurcation points. It is shown that the results obtained through dynamical and bifurcation analysis, including equilibrium states and stability, for this complex mathematical model reveal new behaviors and allow control of essential phenomena, such as the trapping zone, which are often difficult to capture using traditional methods. The numerical method, based on domain decomposition techniques and existing bifurcation software platforms, has been successfully applied to address the challenges posed by the complex channel geometry and the high nonlinearity of the model. Saddle-node bifurcations, periodic orbits, and heteroclinic orbits are essential for providing a framework to characterize recirculating flows and the transitions between different flow states. This technique can be applied to a variety of channel geometries, including, for example [37]

$$R_l(Z,t) = R_{i0} + A_i \sin\big(kZ - \omega t\big),$$
$$R_u((Z,t) = R_{o0} + A_o \sin\big(kZ - \omega t + \varphi\big),$$

or other mathematical models of the channel walls [6, 38]. A key finding of this work is the ability to control the trapping zone, which is influenced by parameters such as the catheter radius ratio, amplitude ratio, Grashof number, heat source or sink, and flow rate. The trapping zone can form in the lower region, upper region, or extend across the entire channel. This makes the results a significant refinement and extension of earlier studies on similar models.

An extension of the present approach will be considered in future work to address cases involving long wavelength δ and higher Reynolds numbers. In such situations, the inertial terms in Eqs (2.5)–(2.8) become significant, leading to fundamentally different flow behavior. Consequently, the current analytical formulation may no longer be applicable, and fully numerical methods would likely be required to accurately capture the flow dynamics.

Author contributions

Both authors contributed equally to this work. Conceptualization, M. A. A. and E. D. E.; methodology, M. A. A. and E. D. E.; formal analysis, M. A. A. and E. D. E.; investigation, M. A. A. and E. D. E.; writing—original draft preparation, M. A. A. and E. D. E.; writing—review and editing. All authors have read and agreed to the published version of the manuscript.

Use of AI tools declaration

The authors declare that they have not used Artificial Intelligence (AI) tools in the creation of this article.

Conflict of interest

The author declares no conflict of interest in this paper.

References

1. S. U. S. Choi, Enhancing thermal conductivity of fluids with nanoparticles, In: *ASME International Mechanical Engineering Congress and Exposition*, American Society of Mechanical Engineers, 1995, 99–105. https://doi.org/10.1115/IMECE1995-0926
2. W. Bian, M. Min, X. Liang, J. Xu, Y. Lou, X. Fan, et al., Investigation on thermal performance and flow characteristics of hybrid nanofluids in uniform and non-uniform twisted oval tubes, *Case Stud. Therm. Eng.*, **76** (2025), 107275. https://doi.org/10.1016/j.csite.2025.107275
3. S. E. Ahmed, A. A. M. Arafa, S. A. Hussein, Biomedical analysis of heat and mass transport in hybrid nanofluid flow with bioconvection and reactive species over an oscillatory curved surface in a spatially varying porous medium, *Int. J. Heat Mass Tran.*, **252** (2025), 127508. https://doi.org/10.1016/j.ijheatmasstransfer.2025.127508
4. J. Du, Y. Wang, W. Yang, J. Wang, Z. Cao, B. Sundén, Effect of nanoparticle concentration and surfactants on nanofluid pool boiling, *Int. J. Heat Mass Tran.*, **221** (2024), 125080. https://doi.org/10.1016/j.ijheatmasstransfer.2023.125080
5. S. Z. H. Shah, H. A. Wahab, S. Ahmad, U. Khan, A. Ishak, E. M. Sherif, et al., Numerical investigation of ternary hybrid non-newtonian nanofluids and heat transport over an inclined shrinking sheet utilizing artificial neural network, *Adv. Math. Phys.*, **1** (2024), 4133538. https://doi.org/10.1155/2024/4133538
6. A. Tanveer, Iram, M. Z. Alqarni, S. Saleem, A. Al-Zubaidi, Enhancement in heat generation through ternary hybrid nanofluid in a periodic channel, *Case Stud. Therm. Eng.*, **69** (2025), 106011. https://doi.org/10.1016/j.csite.2025.106011
7. G. Huminic, A. Huminic, Hybrid nanofluids for heat transfer applications–A state-of-the-art review, *Int. J. Heat Mass Tran.*, **125** (2018), 82–103. https://doi.org/10.1016/j.ijheatmasstransfer.2018.04.059
8. N. S. Akbar, T. Zamir, T. Noor, T. Muhammad, M. R. Ali, Heat transfer enhancement using ternary hybrid nanofluid for cross-viscosity model with intelligent levenberg-marquardt neural networks approach incorporating entropy generation, *Case Stud. Therm. Eng.*, **63** (2024), 105290. https://doi.org/10.1016/j.csite.2024.105290
9. C. Revnic, T. Grosan, I. Pop, Dual solutions of ternary hybrid nanofluids stagnation point over a linearly stretching/shrinking sheet, *J. Therm. Anal. Calorim.*, **150** (2025), 11265–11274. https://doi.org/10.1007/s10973-025-14195-8
10. I. I. Wertgeim, M. A. Zaks, R. V. Sagitov, A. N. Sharifulin, Instabilities, bifurcations, and nonlinear dynamics in two-dimensional generalizations of kolmogorov flow, *Fluid Dyn.*, **57** (2022), 430–443. https://doi.org/10.1134/S0015462822040115
11. M. Bouteraa, C. Nouar, E. Plaut, C. Metivier, A. Kalck, Weakly nonlinear analysis of rayleigh-bénard convection in shear-thinning fluids: nature of the bifurcation and pattern selection, *J. Fluid Mech.*, **767** (2015), 696–734. https://doi.org/10.1017/jfm.2015.64
12. Y. Zhang, L. Xie, Y. Dong, J. Huang, S. Ruan, Y. Takeuchi, Bifurcation analysis in a tumor-immune system interaction model with dendritic cell therapy and immune response delay, *SIAM J. Appl. Math.*, **83** (2023), 1892–1914. https://doi.org/10.1137/22M1533979

13. D. Das, B. L. Sharma, Local bifurcation analysis of circular von-kármán plate with kirchhoff rod boundary, *SIAM J. Appli. Math.*, **85** (2025), 1749–1784. https://doi.org/10.1137/24M1703999

14. Beenish, M. Samreen, Analytical solutions and dynamical insights of the modified benjamin-bona-mahony equation with applications in nonlinear optics, *J. Appl. Math. Comput.*, **71** (2025), 699–723. https://doi.org/10.1007/s12190-025-02484-2

15. Y. Xiao, Z. Jiang, P. Meng, W. Yin, D. Qi, L. Zhou, Local manifold approximation of dynamical system based on neural ordinary differential equation, *Physica D*, **477** (2025), 134688. https://doi.org/10.1016/j.physd.2025.134688

16. J. M. Cadou, M. Potier-Ferry, B. Cochelin, A numerical method for the computation of bifurcation points in fluid mechanics, *Eur. J. Mech. B/Fluid.*, **25** (2006), 234–254. https://doi.org/10.1016/j.euromechflu.2005.07.002

17. H. A. Dijkstra, F. W. Wubs, A. K. Cliffe, E. Doedel, I. F. Dragomirescu, B. Eckhardt, et al., Numerical bifurcation methods and their application to fluid dynamics: Analysis beyond simulation, *Commun. Comput. Phys.*, **15** (2014), 1–45. https://doi.org/10.4208/cicp.240912.180613a

18. J. S. Keeler, J. E. Sprittles, Finding the point of no return: Dynamical systems theory applied to the moving contact-line instability, *Curr. Opin. Colloid In.*, **67** (2023), 101724. https://doi.org/10.1016/j.cocis.2023.101724

19. H. A. Hosham, E. N. Thabet, A. M. Abd-Alla, S. M. M. El-Kabeir, Dynamic patterns of electroosmosis peristaltic flow of a Bingham fluid model in a complex wavy microchannel, *Sci. Rep.*, **13** (2023), 8686. https://doi.org/10.1038/s41598-023-35410-2

20. K. Ullah, N. Ali, Stability and bifurcation analysis of stagnation/equilibrium points for peristaltic transport in a curved channel, *Phys. Fluids*, **31** (2019), 073103. https://doi.org/10.1063/1.5097555

21. N. Ali, H. R. Kazmi, K. Ullah, A study on the bifurcation of the peristaltic driven flow of Ellis fluid, *Wave. Random Complex*, **2023** (2023), 1–18. https://doi.org/10.1080/17455030.2023.2179338

22. H. A. Hosham, N. M. Hafez, Bifurcation phenomena in the peristaltic transport of non-Newtonian fluid with heat and mass transfer effects, *J. Appl. Math. Comput.*, **67** (2021), 275–299. https://doi.org/10.1007/s12190-020-01477-7

23. H. A. Hosham, N. M. Hafez, Global dynamics and bifurcation analysis for the peristaltic transport through nonuniform channels, *J. Comput. Nonlinear Dyn.*, **17** (2022), 061001. https://doi.org/10.1115/1.4053668

24. N. Ali, K. Ullah, H. Rasool, Bifurcation analysis for a two-dimensional peristaltic driven flow of power-law fluid in asymmetric channel, *Phys. Fluids*, **32** (2020), 073104. https://doi.org/10.1063/5.0011465

25. I. Shahzadi, N. Ahsan, S. Nadeem, A. Issakhov, Analysis of bifurcation dynamics of streamlines topologies for pseudoplastic shear thinning fluid: Biomechanics application, *Physica A*, **540** (2020), 122502. https://doi.org/10.1016/j.physa.2019.122502

26. H. M. Sayed, H. A. Hosham, Dynamics and bifurcations of non-Newtonian Au-Cu/blood hybrid nanofluid model of electrokinetic flow in asymmetrically tapered wave microchannel, *Wave. Random Complex*, **35** (2025), 6496–6513. https://doi.org/10.1080/17455030.2022.2078018

27. M. G. Thoubaan, D. G.S. Al-Khafajy, A. K. Wanas, D. Breaz, L. Cotîrlă, Analysis of a bifurcation and stability of equilibrium points for jeffrey fluid flow through a non-uniform channel, *Symmetry*, **16** (2024), 1144. https://doi.org/10.3390/sym16091144

28. H. Rasool, N. Ali, K. Ullah, Bifurcations of streamlines in peristaltic flow without lubrication approximation: A case study, *ZAMM J. Appl. Math. Mech.*, **104** (2024), e202200345. https://doi.org/10.1002/zamm.202200345

29. Z. Abbas, R. Mehboob, M. Y. Rafiq, S. Khaliq, A. Ali, Peristaltic pumping of ternary hybrid nanofluid between two sinusoidally deforming curved tubes, *Adv. Mech. Eng.*, **15** (2023), 16878132231189373. https://doi.org/10.1177/16878132231189373

30. M. A. El Kot, E. M. Elsaid, Y. Abd Elmaboud, A. M. Algatheem, M. R. Eid, Beyond shear-thinning hyperbolic tangent electromagnetic nanofluid flow-based blood in porous constricted channels: Electroosmotic and activation energy dynamics, *Mod. Phys. Lett.*, **40** (2026), 2550280. https://doi.org/10.1142/S021798492550280X

31. A. Khan, Hashim, M. Farooq, S. M. Hussain, H. Ahmad, W. Jamshed, et al., Convective heat transfer in ternary nanofluids over stretching sheets under radiation and slip conditions, *J. Radiat. Res. Appl. Sci.*, **18** (2025), 101974. https://doi.org/10.1016/j.jrras.2025.101974

32. K. Smida, Adnan, M. U. Sohail, I. Tlili, A. Javed, Numerical thermal study of ternary nanofluid influenced by thermal radiation towards convectively heated sinusoidal cylinder, *Heliyon*, **9** (2023), e20057. https://doi.org/10.1016/j.heliyon.2023.e20057

33. H. Aybar, M. Sharifpur, M. R. Azizian, M. Mehrabi, J. P. Meyer, A review of thermal conductivity models for nanofluids, *Heat Transfer Eng.*, **36** (2015), 1085–1110. https://doi.org/10.1080/01457632.2015.987586

34. W, Yu, S. Choi, The role of interfacial layers in the enhanced thermal conductivity of nanofluids: A renovated maxwell model, *J. Nanopart. Res.*, **5** (2004), 355–361. https://doi.org/10.1007/s11051-004-2601-7

35. A. H. Shapiro, M. Y. Jaffrin, S. L. Weinberg, Peristaltic pumping with long wavelengths at low reynolds number, *J. Fluid Mech.*, **37** (1969), 799–825. https://doi.org/10.1017/S0022112069000899

36. W. J. F Govaerts, *Numerical methods for bifurcations of dynamical equilibria*, Society for Industrial and Applied Mathematics, 2000.

37. K. Thirunavukarasan, G. Sucharitha, Thermal performance and mhd peristaltic flow of hybrid nanofluid (au-ta/blood) in an asymmetric conduit with electro-osmosis and shape factor effects, *Case Stud. Therm. Eng.*, **66** (2025), 105708. https://doi.org/10.1016/j.csite.2024.105708

38. M. A. A. Mohamed, Peristaltic eyring-powell nanofluid flow linking with microorganisms across a curved channel: Maa mohamed, *Theor. Comput. Fluid Dyn.*, **39** (2025), 33. https://doi.org/10.1007/s00162-025-00751-3

AIMS Press